Low-latitude boundary layer clouds as seen by CALIPSO

Brian Medeiros,[1,2] Louise Nuijens,[1] Chiara Antoniazzi,[1] and Bjorn Stevens[1,3]

Received 30 April 2010; revised 2 August 2010; accepted 20 September 2010; published 4 December 2010.

[1] The distribution of low-level cloud in the tropical belt is investigated using 6 months of Level 2 retrievals from Cloud-Aerosol Lidar and Infrared Pathfinder Satellite Observation (CALIPSO) at 333 m and 1 km horizontal resolutions. Regional patterns of tropical clouds emerge from the data, matching expectations from existing observations. The advantage of the lidar is highlighted by the distribution of cloud-top height, revealing the preponderance of low-level clouds over the tropical oceans. Over land, cloud top is more uniformly distributed under the influence of diurnal variation. The integrated cloud-top distribution suggests tropical, marine low-cloud amount around 25–30%; a merged CALIPSO-CloudSat product has a similar cloud-top distribution and includes a complementary estimate of cloud fraction based on the lidar detections. The low-cloud distribution is similar to that found in fields of shallow cumulus observed during the Rain in Cumulus Over the Ocean (RICO) field study. The similarity is enhanced by sampling near the RICO site or sampling large-scale conditions similar to those during RICO. This finding shows how satellite observations can help to generalize findings from detailed field observations.

Citation: Medeiros, B., L. Nuijens, C. Antoniazzi, and B. Stevens (2010), Low-latitude boundary layer clouds as seen by CALIPSO, *J. Geophys. Res.*, *115*, D23207, doi:10.1029/2010JD014437.

1. Introduction

[2] Low-level clouds are ubiquitous over tropical and subtropical oceans, taking familiar forms like homogeneous stratocumulus and trade-wind cumulus, and also intermediate forms like cumulus rising into stratocumulus. These boundary layer clouds form under the descending branches of the Hadley and Walker circulations with cloud top below the freezing level and often near the trade inversion. Earth's energy and hydrologic cycles feel the impact of these clouds, for example through the shortwave effects of stratocumulus [*Hartmann et al.*, 1992] or trade-wind cumulus preconditioning the atmosphere for deep, moist convection [*Neggers et al.*, 2007]. Because these clouds are small and/or thin, they must be parameterized in conventional climate models. However, climate models produce very different cloud statistics in these regimes, and the response of these clouds to a changing climate is inconsistent among models [*Cess et al.*, 1989; *Bony et al.*, 2004; *Medeiros et al.*, 2008]. Parameterizations for boundary layer clouds must be improved to bolster confidence in estimates of climate sensitivity, and such improvements should be guided by observations.

[3] Active remote sensors provide new opportunities to quantify the structure of boundary layer clouds, and guide improvements in cloud parameterizations. Previous global observations of clouds have been limited to passive visible and infrared imager data, which struggle to resolve small boundary layer clouds and lack information about vertical structure [*Stephens et al.*, 2002]. One active sensor of particular interest for boundary layer clouds is the CALIOP lidar aboard the Cloud-Aerosol Lidar and Infrared Pathfinder Satellite Observation (CALIPSO) satellite. The CALIOP is sensitive to the presence of thin cloud layers, and its small footprint (as little as 333 m) can identify small boundary layer clouds, especially in the absence of optically thick, high clouds where low clouds most dramatically impact the fluxes of shortwave radiation.

[4] In the present work, we explore the emerging climatology of cloud-top height from two CALIPSO cloud products, emphasizing low-level clouds. Besides describing the horizontal and vertical cloud-top distribution, we investigate the relationships between the actively sensed cloud tops with the existing International Satellite Cloud Climatology Project (ISCCP) as well as with measurements from an airborne lidar that was flown over fields of shallow cumulus clouds during the recent Rain in Cumulus Over the Ocean (RICO) field campaign. We show that the cloud distribution from these products contains geographic patterns similar to other satellite estimates and that the vertical distribution is consistent with the structure observed during RICO. The similarity to the other observations adds value to existing satellite data sets by validating some aspects of their climatology. By capturing similar statistics to those obtained from our field study, we are encouraged to use CALIPSO data to generalize findings from spatially and temporally

[1]Department of Atmospheric and Oceanic Sciences, University of California, Los Angeles, California, USA.
[2]National Center for Atmospheric Research, Boulder, Colorado, USA.
[3]Max Planck Institute for Meteorology, Hamburg, Germany.

0148-0227/10/2010JD014437

Table 1. Number of Detected Cloud Layers in the CALIPSO 333 m Product for Three Sampling Strategies[a]

		Tropical Ocean	RICO Area	Broader Trades
Total Points	$\sum_{j=0}^{N_{max}} N_j$	67,451,788	87,849	2,394,154
No Layers	N_0	42,614,674	64,072	1,576,094
1 Layer	N_1	22,617,456	21,485	735,854
2 Layers	N_2	2,047,033	2109	76,028
2 Layers ($\delta Z > 1$ km)		681,757	553	23,918
>2 Layers	$\sum_{j=3}^{N_{max}} N_j$	172,625	183	6178

[a]The total number of two detected layers are supplemented with the number of two-layer detections in which the cloud tops are separated by at least 1 km ($\delta Z > 1$ km). The left column corresponds to equation (2).

limited field studies to much larger scales. To provide more perspective into the CALIPSO data, we investigate cloud distributions from a merged product using CALIPSO and the cloud-profiling radar (CPR) aboard CloudSat called 2B-GEOPROF-Lidar [*Mace et al.*, 2009].

[5] The remainder of this paper is structured as follows: section 2 reviews the CALIPSO data that we use and describes our simple approach to analyzing the data. An overview of the results is presented in section 3, showing the horizontal and vertical distribution of low clouds from the CALIPSO products. Section 4 focuses on the comparison with the lidar measurements from RICO, and section 5 turns to the merged radar-lidar product. A discussion and summary of our findings is provided by section 6.

2. Data and Methods

2.1. Satellite Data

[6] The primary data set used here is from the Cloud-Aerosol Lidar with Orthogonal Polarization (CALIOP) aboard CALIPSO. Part of the "A-Train" constellation, CALIPSO follows a Sun-synchronous orbit with an equatorial crossing time around 0130 and 1330 local time (LT). The CALIOP fires laser pulses at two wavelengths about 20 times per second (532 and 1064 nm at 20.16 Hz) and measures the backscatter intensity at the same wavelengths (including two orthogonally polarized components at 532 nm). An adaptive threshold technique that accounts for the varying signal to noise ratio with height and location is used to detect cloud and aerosol layers from the backscattered signal [*Vaughan et al.*, 2004; *Winker et al.*, 2008]. The CALIPSO mission has been collecting data since June 2006.

[7] The CALIPSO products used here are the Version 2.01 Level 2 data sets (http://eosweb.larc.nasa.gov/PRODOCS/calipso/table_calipso.html) at horizontal resolutions of 333 m and 1 km. The former represents a single lidar shot, while the latter is the average of three shots, both from 5 km scenes in which the layer detection algorithm identifies at least one cloud layer [*Winker et al.*, 2008]. The 333 m data use a vertical domain from 8.2 km to the surface, while the 1 km product extends from 19 km to the surface. Both data sets have a vertical resolution of 30 m below 8.2 km. Above 8.2 km, the 1 km product degrades its vertical resolution to 60 m. Both of these limitations are imposed to decrease the downlink bandwidth from the satellite [*Winker et al.*, 2003]; the artificial cutoff at 8.2 km in the 333 m product introduces biases in some cloud statistics which are discussed below. These products include the number of cloud layers detected and the cloud-top height of those layers: these are the quantities discussed in this study. These products are liable to overlook the most tenuous cloud layers (e.g., subvisible cirrus) because of under sampling, but since the focus here is on low-level clouds that are expected to be optically thick, this should not severely bias the statistics; in fact, by excluding tenuous layers and focusing on more robust features, we expect reliable statistics from the low-level cloud layers. The 5 km cloud layer product, not used here, includes more information about optically thin layers in the upper troposphere.

[8] The retrieval algorithms determine the number of cloud layers, from zero to either five for the 333 m product or ten for the 1 km product, and each layer has an associated layer top height. Because of the strong attenuation of the lidar signal through cloudy air, the chance of detecting additional cloud layers drops dramatically with increasing numbers of layers (e.g., Table 1), and CALIPSO can miss low-level clouds below high clouds [e.g., *Kahn et al.*, 2008; *Marchand et al.*, 2008]. Lidar signals are fully attenuated by clouds with optical depth ≥ 3, which is much greater than most upper-level cirrus but is common for boundary layer clouds; when multiple cloud layers are present, the signal attenuation is cumulative, leading to enhanced uncertainties in retrieving lower layers [cf. *Winker et al.*, 2009]. Though the retrieval algorithm includes adjustments to the attenuated scattering ratio after each detected layer, allowing detection of lower layers despite attenuation, layer identification degrades with the decreased signal strength [*Vaughan et al.*, 2009]. In light of the increased uncertainties, we particularly focus on detections of single cloud layers, which are the majority of cloud detections. Detections with two (or more) cloud layers are examined for comparison. Additional details of the layer detection scheme are provided by *Vaughan et al.* [2009].

[9] The 2B-GEOPROF-Lidar version 1.1 (release R04, hereafter RL-GEOPROF) product combines lidar information from CALIPSO with CloudSat's CPR (the 94 GHz Cloud Profiling Radar; details can be found at www.cloudsat.cira.colostate.edu), providing another view of the clouds. CloudSat follows the same orbit as CALIPSO, and they observe the same location (with a different footprint) within about 15 s of each other. In principle, the overlapping information gathered from the two instruments can improve the fidelity of cloud detection by exploiting the strengths of each instrument. Because the CPR and CALIOP have different footprints, the RL-GEOPROF product has the same spatial resolution as the CPR (0.2–1.4 km across track, 1.7–2.5 km along track and 0.24 km in vertical [*Marchand et al.*, 2008]). The combined product includes the number of detected layers, their locations, and the fraction of lidar volumes reporting cloud in each radar volume.

[10] For both CALIPSO and RL-GEOPROF, 6 months of data are analyzed, covering two Northern Hemisphere winter seasons (DJF, December 2006 (2007) to February 2007 (2008)). The DJF season was chosen because it corresponds to the period of study during the RICO field campaign in the northwestern Atlantic tradewinds. Night and day and land and ocean are considered separately initially. Identifying cloud layers is more error prone in the presence of the daytime solar background signal. A day-night bias has been identified [*Winker et al.*, 2008], but this bias should not impact detection of low and/or optically thick ($\tau > 0.1$) clouds. Focusing on the low clouds over the ocean, we show little difference between the day and night distributions, and because of this, much of the following analysis combines day and night data. We include latitudes from 30°S to 30°N in what we loosely define as the tropical belt.

2.2. Rain in Cumulus Over the Ocean

[11] The RICO field campaign observed a typical trade-wind region in the western Atlantic Ocean, upstream of Antigua and Barbuda during undisturbed wintertime conditions during December 2004 and January 2005 [*Rauber et al.*, 2007]. A wide range of cloud and aerosol measurements were collected during RICO, including observations using the NCAR scanning aerosol backscatter lidar (SABL) mounted on the NCAR C-130 aircraft. The lidar detects cloud top and edges, like the CALIOP, but without suffering obscuring effects of upper-level clouds.

[12] The CALIPSO and RICO observations do not overlap in time, but as the weather conditions during RICO were typical of the undisturbed trades [*Rauber et al.*, 2007], we compare cloud observations from RICO with measurements by CALIPSO to explore whether the satellite data offers an opportunity to generalize from the intensive observations by using a large sample population.

[13] Cloud-top height from SABL data is derived from 35 circular flight patterns of about 200 km in circumference near 4.5 km altitude. A threshold value of 18 dB in the backscattered signal is applied here to define a cloud detection. This value is similar to other uses of the SABL data [cf. *Medeiros and Stevens*, 2010; *Nuijens et al.*, 2009]. There is a sensitivity in the estimate of cloud fraction to the choice of threshold, especially near cloud base where one finds many small clouds, or cloud fragments, and significant scattering from deliquesced aerosol. Higher threshold values result in lower estimates of cloud fraction.

2.3. Deriving Cloud Statistics

[14] All cloud statistics presented here are determined as simply as possible, with as little filtering as is practical. For example, an initial estimate of cloud fraction ($\mathcal{C}$) for both CALIPSO products (1 km and 333 m) is determined by simple counting of cloud-top incidence within 2.5° latitude-longitude boxes: the number of scanned profiles with at least one cloud layer (N_{Cld}) is divided by the total number of lidar scans (N_{Tot}),

$$\mathcal{C} = \frac{N_{\mathrm{Cld}}}{N_{\mathrm{Tot}}}. \tag{1}$$

The result is shown in Figures 1 and 2 for the 333 m and 1 km products, respectively. Subsequent analysis retains this simple approach; placing the data on a grid is omitted except for comparison to gridded data (i.e., ISCCP) or to sample based on location.

[15] Distributions of cloud-top height are derived by using 250 m bins in the vertical. This is more coarse than the 30 m resolution of the CALIPSO products, but is similar to that of the oversampled CloudSat radar data. The cloud-top frequency is calculated as

$$\mathrm{Z}_i(z) = \frac{N_i(z)}{\sum_{j=0}^{N_{\max}} N_j}, \tag{2}$$

where $\mathrm{Z}_i(z)$ is the frequency of cloud top in the height bin centered at z with i cloud layers detected, N_i is the number of detections with i cloud layers, N_j is the number of detections with j detected layers, and $N_{\max}$ is the maximum number of cloud layers allowed by the algorithm (i.e., 5 for the 333 m product, 10 for the 1 km product). A low-cloud amount can be estimated from the derived cloud-top height distribution by integrating downward; in the analysis below, the height where the integration begins is chosen to be 3 km. The cloud-top frequency in equation (2) is sensitive to the chosen bin size, but the effect is roughly linear: decreasing the bin size to 125 m approximately halves the frequency, while increasing it to 500 m smoothes the features and nearly doubles the frequency. The vertically integrated cloud amount, however, shows little dependence on bin size because the total number and height of detections does not depend on the sampling.

3. CALIPSO's View of Tropical Clouds

[16] This section gives an overview of the tropical cloud distribution in the CALIPSO products.

3.1. Geographical Distribution

[17] Six months of CALIPSO data provides a large sample, shown compiled in 2.5° × 2.5° grid boxes in Figures 1 and 2. The maps also present the spatial structure of the CALIPSO cloud detections, which are dominated by single cloud layers (e.g., Table 1). Table 1 also shows the decreasing likelihood of detecting additional cloud layers. A table for the 1 km product is similar to Table 1, but with one third the total data and a higher fraction of detections with one layer (see section 3.3).

[18] Even with just two DJF seasons, the CALIPSO products show familiar patterns of tropical cloud (Figures 1 and 2). Marine stratus clouds are identifiable near cold eastern boundary currents by frequent cloud detection with low cloud tops. Regions of deep convection are also identified as cloudy, but with high tops. The 1 km product better detects these higher clouds, showing more frequent cloud detection and higher average cloud-top height than the 333 m product which reports zero cloud in the presence of optically thick clouds (roughly $\tau > 3$) above the 8.2 km cutoff. Trade-wind regions, like the site of the RICO study in the western Atlantic, can be identified as oceanic regions where cloud detections are relatively rare (<50% in the 1 km product) and cloud top is low (<5 km in the 1 km product). Higher cloud top over land is also apparent in both products.

[19] To evaluate the spatial distribution of tropical clouds, we compare with the ISCCP distribution of low-cloud

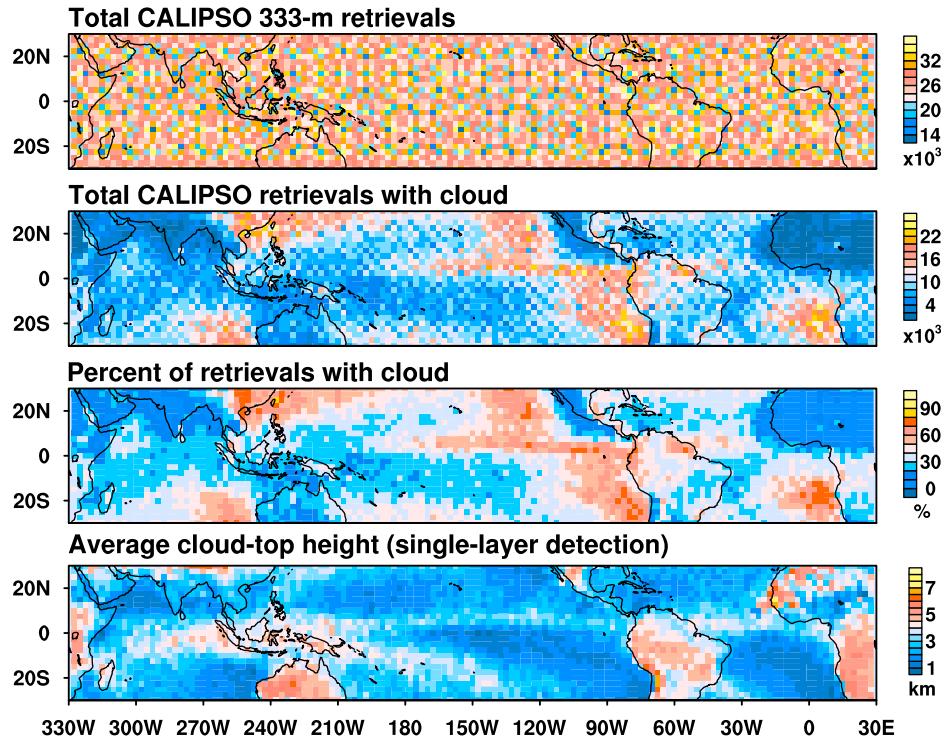

Figure 1. Geographical distribution of (from top to bottom) number of lidar returns (N_{Tot}), the number of returns with cloud detected (N_{Cld}), the percent of returns with cloud detected (C), and average cloud top height (Z) for returns with a single cloud layer for the DJF seasons of 2006-2007 and 2007-2008 from the CALIPSO 333 m product.

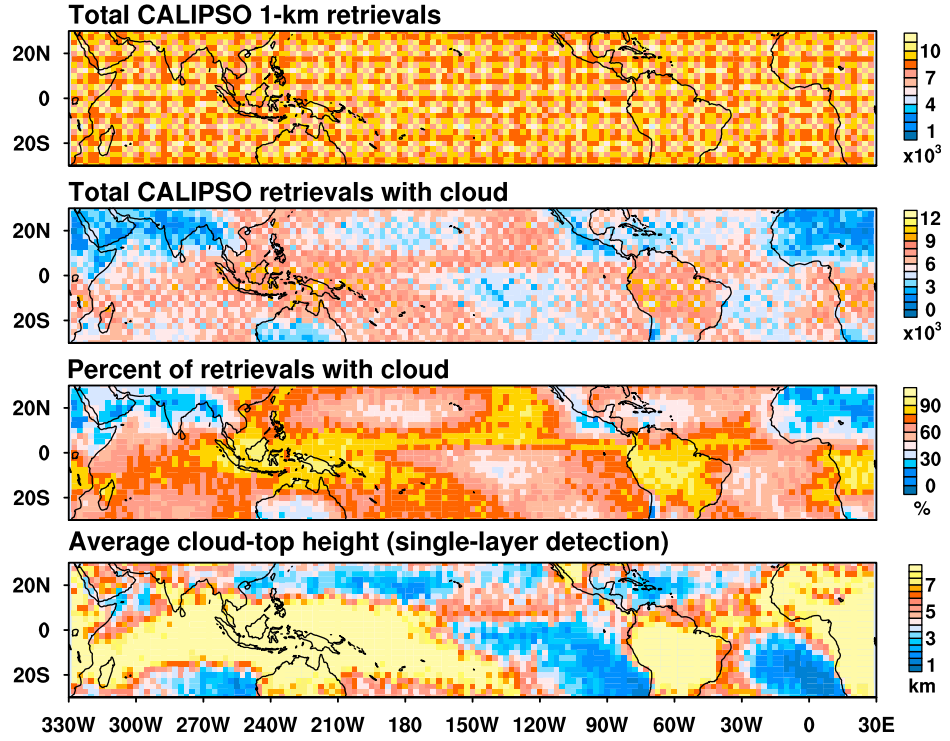

Figure 2. Same as Figure 1 but using the 1 km product, which is more sensitive to high clouds. The scale in the first panel is 3 times smaller than in Figure 1 to account for the averaging used in deriving the 1 km product.

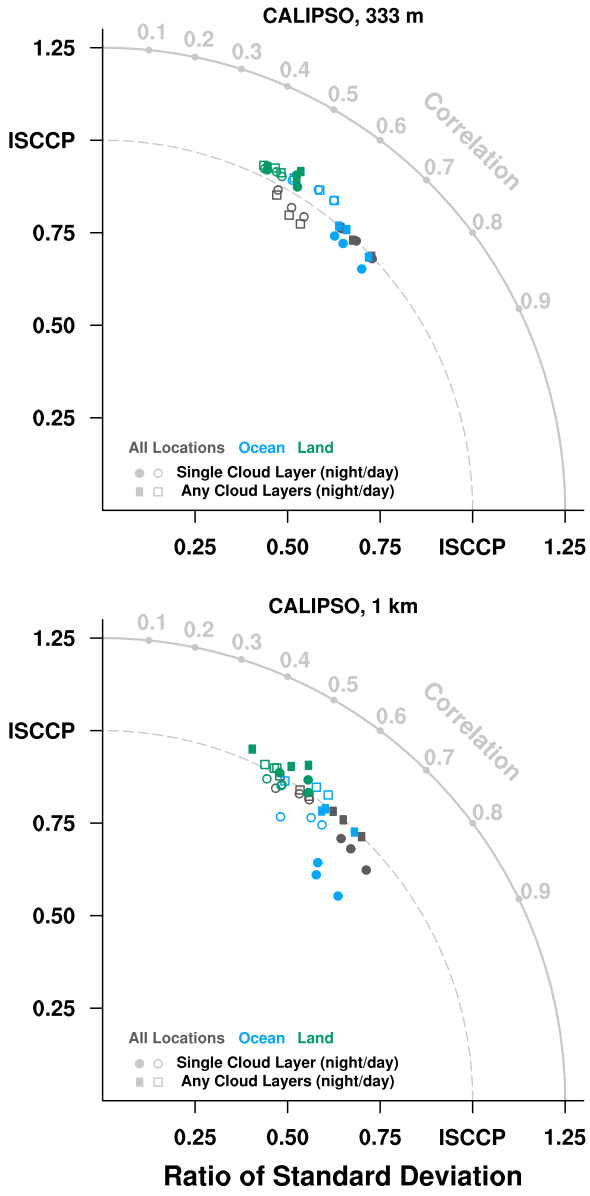

Figure 3. Taylor diagrams comparing the CALIPSO (top) 333 m product and (bottom) 1 km product with the ISCCP D2 low-cloud amount. The radial distance from the origin gives the ratio of the CALIPSO to ISCCP standard deviation, and correlation is plotted as the azimuthal direction (correlation is the cosine of the azimuthal angle). Colors denote geographic sampling (gray is all points, blue is ocean, and green is land). Solid symbols are nighttime CALIPSO data, open are daytime. Circles use CALIPSO detections of a single cloud layer, while squares show all low cloud detected by CALIPSO. There are three of each combination of color and shape, showing 1 month of data each; the months tend to be close together so they are not identified individually.

amount. The ISCCP D2 data set [*Rossow and Schiffer*, 1999] (http://isccp.giss.nasa.gov) is used to generate monthly mean low-cloud amount; clouds are considered low if their tops are at or below the 680 hPa level. As of writing, the D2 data are available through mid-2007, so the comparison here uses 3 months: December 2006 through February 2007. To compare each month, a monthly mean low-cloud amount is constructed from the CALIPSO products using the ISCCP square grid; within each grid cell the fraction of points with $Z \leq 3$ km defines low-cloud amount. This is lower than the 4 km threshold from *Leon et al.* [2008] but appears sufficient to capture most low-level cloud. For each of the 3 months, the low-cloud amounts are compared by determining the pattern correlation, with the results presented by Taylor diagrams in Figure 3. The correlation is calculated using land and ocean together and separately for each month, as well as using single-layer detections and all cloud detections. The azimuthal angle in Figure 3 shows the correlation between CALIPSO and ISCCP, where it is seen that the correlation over ocean is better than over land. The correlation between CALIPSO's single cloud layer detections and ISCCP low-cloud amount is higher than for detections with any number of layers. This is not surprising given that the passive sensors used for ISCCP are not equipped to detect multiple cloud layers, and CALIPSO's lidar becomes attenuated through thicker layers. Nighttime CALIPSO data is better correlated with ISCCP than daytime; it seems unlikely that CALIPSO's known day-night bias is the source of this difference since that bias mostly affects optically thin clouds, and may instead represent a bias in the infrared retrievals that form the basis for nighttime low-cloud detection by ISCCP. The radial coordinate in Figure 3 shows the ratio of the standard deviations, which are generally close to unity, suggesting the data sets have similar variability. The level of correlation between these data sources demonstrates their similar patterns of low cloud, particularly over the ocean, and provides confidence for interpreting the low-cloud statistics of both data sets.

3.2. Vertical Distribution

[20] Distributions of cloud-top height, Z, are shown in Figure 4 for cases when a single cloud layer is detected. The distributions are standardized by the total number of returns (equation (2)), so they show the frequency of detecting a single cloud layer at a given height. Figure 4 is divided into land (Figures 4a and 4c) and ocean (Figures 4b and 4d) for both the 333 m and 1 km products. Since the 333 m product is limited to the lowest 8.2 km and because the main interest here is on low clouds, we clip the distributions in Figure 4 at this height. An estimate of high-cloud amount in the 1 km product is included, reporting the integrated cloud-top distribution above 8.2 km. Daytime and nighttime distributions are shown as open and solid circles, respectively, and the combination is shown by the solid curve. Comparing land and ocean, there is a striking contrast, hinted at by Figures 1 and 2. The ocean distributions show small day-night differences with a single peak centered at 1–2 km, and little cloud above 3 km. More variation between day and night is apparent in the land distribution, which is bimodal in the 333 m product. The bimodal distribution arises because high clouds prevail at night over land while low clouds are more common during the day. The daytime peak, around 2–3 km, is higher than the peak in marine clouds. The 1 km product shows a similar diurnal contrast near 3 km, and cloud tops detected above 9 km increase at night.

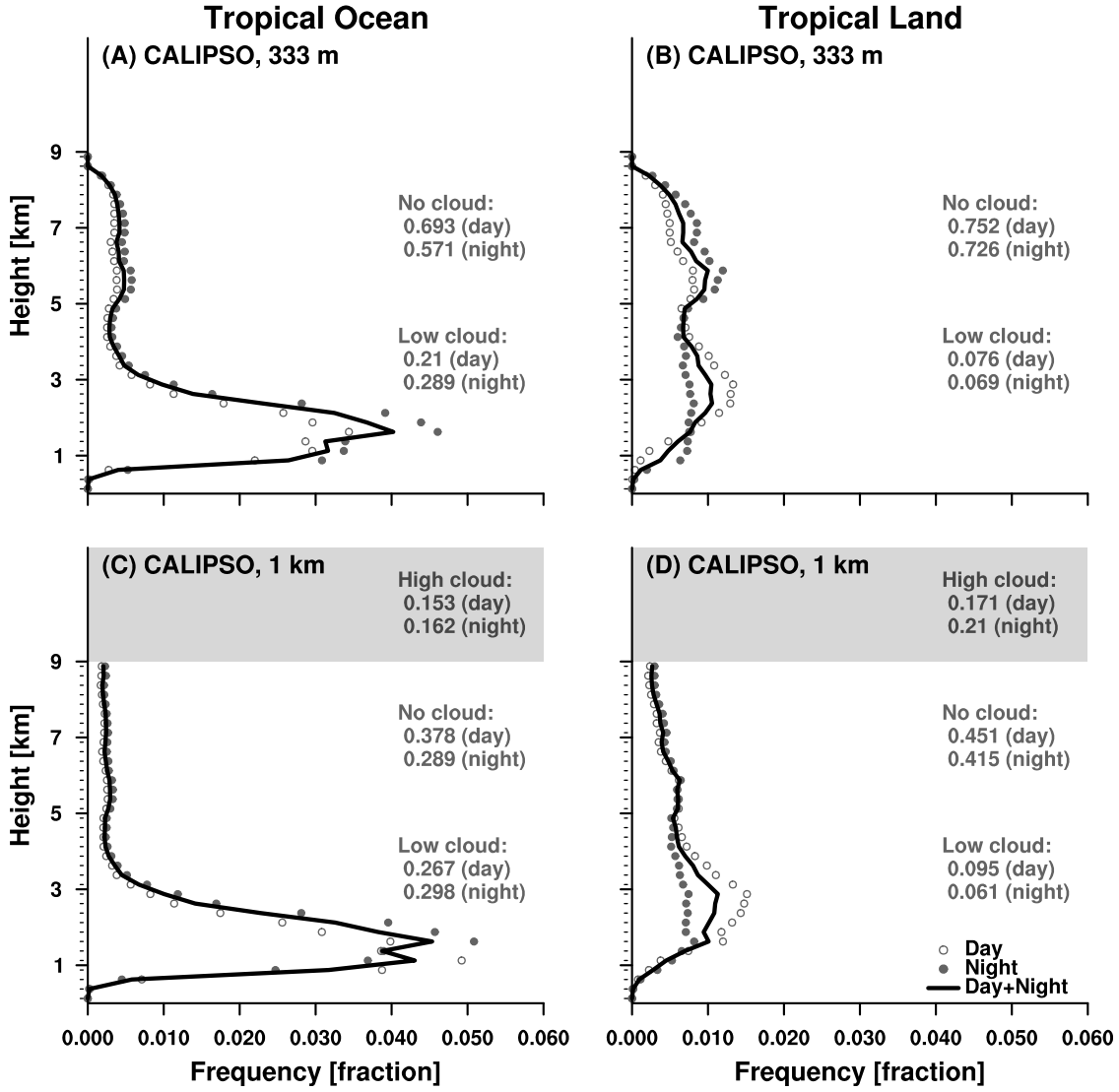

Figure 4. Distribution of cloud top height (250 m bins marked by minor ticks on vertical axis) when a single cloud layer is detected, divided by (a and c) ocean and (b and d) land for the 333 m product (Figures 4a and 4b) and the 1 km product (Figures 4c and 4d). In each panel, open circles show the daytime distribution, solid circles the nighttime, and the solid curve is the combination. The frequency is with respect to the total number of profiles, including those with no cloud (reported as text in each panel). Low-cloud fraction (integrated from 3 km to surface) is shown as well, as is high cloud fraction (>9 km) for the 1 km product.

[21] The distributions of Figure 4, like the geographical distributions of Figure 1, largely conform to expectations of tropical clouds. Over land, diurnal changes in surface fluxes strongly influence the depth and frequency of convection. The tropical oceans are dominated by shallow cumulus clouds, which have a small cloud fraction and cloud tops mostly below the freezing level. Both products hint at an enhancement near 5 km, probably reflecting processes within the freezing/melting layer; a similar feature has also been reported in CALIPSO and other satellite-derived cloud products by *Wu et al.* [2009].

[22] The oceanic distributions in Figure 4 resemble those reported for other analyses of CALIPSO products [*Winker et al.*, 2008; *Leon et al.*, 2008] and for CloudSat [*Haynes and Stephens*, 2007]. *Leon et al.* [2008] focus on regions with large low-cloud amount, defined using $Z \leq 4$ km, and show slightly lower low-level cloud tops in the 1 km product. On the other hand, *Winker et al.* [2008] estimate global cloud fraction from the 5 km product, showing cloud fraction maximizing around 500 m at >25%. The cloud-top distributions in Figure 4 differ from the previous analyses by including the clouds across the entire tropics, but separating land and ocean and excluding the extratropical clouds.

[23] When two well-separated cloud layers are detected (Figure 5), the distribution of cloud top for the lower layer is qualitatively similar to the single-layer detections (Figure 4). Well-separated cases (in which layers are at least 1 km apart; see also Table 1) are used because the CALIPSO products tend to detect multiple layers in close proximity. When the layers are separated, differences in the distribu-

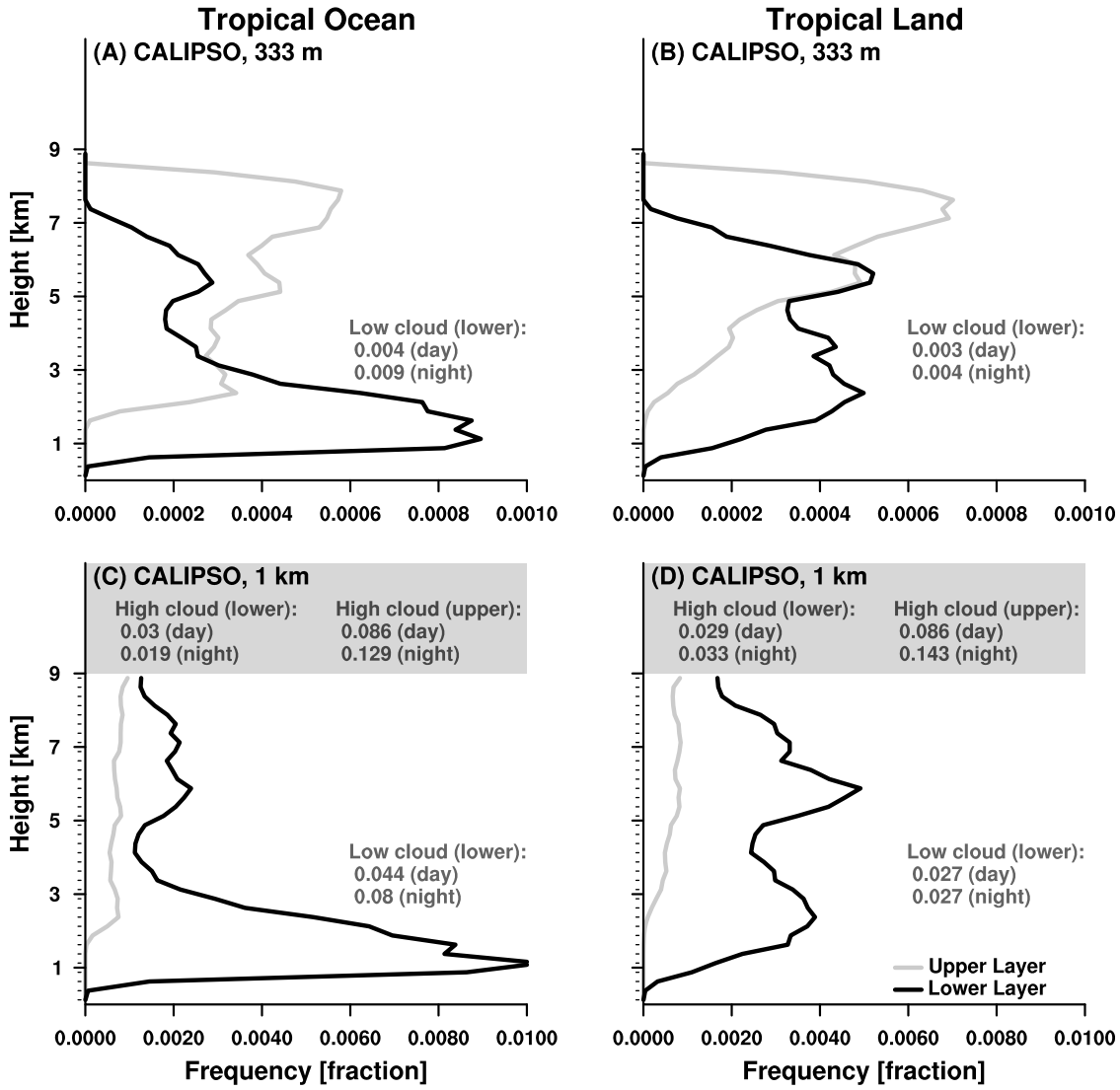

Figure 5. Distribution of cloud top height when two well-separated cloud layers are detected. Black curves show the distribution of the lower of the two layers, and gray shows the upper layer. Day and night are combined; otherwise conventions are as in Figure 4 but the horizontal scale is reduced and is different for the two products. The summation of each curve is the frequency of detecting two cloud layers separated by at least 1 km; the black and gray curves in each panel have the same sum, but those sums are different among the four panels.

tions emerge, as shown in Figure 5. The 333 m product (Figures 5a and 5b) shows the upper level cloud maximizing near the 8.2 km upper limit, while the 1 km product's higher layer suggests 8–14% high-cloud amount. The lower layer shows more low-level cloud (4–8%) than high cloud (2–3%). This inspires the image of high, thin cirrus overlying shallow cumulus. The secondary maximum around 6 km in the lower layer might be suggestive of more disturbed conditions or stratiform cloud near the freezing level. The land distributions are similar, but as in Figure 4, diurnal variation broadens the cloud-top distribution.

3.3. Sensitivity to Resolution

[24] As discussed by *Winker et al.* [2008], single CALIOP laser shots have a small signal-to-noise ratio, and averaging several laser shots together enhances the sensitivity to more tenuous cloud layers. The 5 km product averages 15 laser shots to improve the sensitivity, and *Winker et al.* [2008] show initial results with that product, including the vertical distribution of global cloud coverage for 1 month. Those results show larger cloud coverage than Figure 4. While several factors play into the apparent difference, like combining ocean and land, including extratropical regions, and the larger sensitivity of the 5 km product to thin cloud layers, it is also a result of differences in the construction. Figure 4 shows the probability of detecting cloud top; integrating the distributions give similar values for low-cloud amount to that of *Winker et al.* [2008].

[25] There are also some differences between the 1 km and 333 m products, as seen in both the geographic patterns (Figures 1 and 2) and the vertical distribution of cloud-top height (Figures 4 and 5). The first panel in Figures 1 and 2

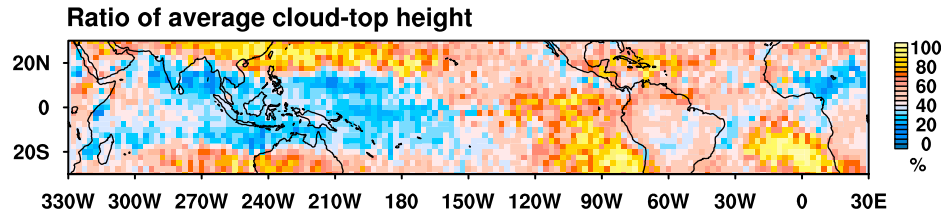

Figure 6. Ratio of the average cloud top height in the 333 m to the 1 km products.

has a scale that differs by a factor of 3, producing nearly identical maps, because of the averaging used to create the 1 km product. The number of retrievals detecting cloud layers do not differ by the same factor of three because the 1 km product detects clouds above the 8.2 km limit of the 333 m product. The 1 km product detects about 40–50% as many retrievals with cloud layers as the 333 m product in regions of large-scale subsidence and predominantly low-level clouds, and more than the 333 m product in regions of high clouds. In the presence of high, thick clouds that attenuate the lidar beam, the 333 m product reports zero cloud layers, so the number of cloud detections and the fraction of cloudy detections in areas of deep convection is relatively small (Figure 1). This bias is highlighted by Figure 6, which shows the ratio of average cloud-top height between the products. The western Pacific shows the largest difference because of extensive high-level clouds. In contrast to regions of high clouds are the subsiding regions where both products detect similar cloud-top height with nearly the same frequency.

[26] Another effect of the height limit on the 333 m product compared to the 1 km product is fewer detections with multiple cloud layers. This difference is evident in Figure 5 where there is a factor of 10 difference in the scale between the products' distributions. The apparent difference is exaggerated by two other factors: first, detections with two well-separated layers are less common in the 333 m product compared to the 1 km one. The 333 m product is more prone to reporting cloud layers in close vertical proximity to each other; about one third of the two-layer detections have the layers separated by at least 1 km, compared with nearly all of them in the 1 km product. A second potential contribution to the discrepancy between the frequency of multilayer detections is that the 1 km product can detect nonoverlapping clouds with different cloud-top heights as multiple layers because of the spatial averaging of several lidar shots, whereas the 333 m product only detects multiple layers when they are within a single lidar shot.

4. Comparison With RICO

[27] Tropical clouds appear to be dominated by shallow clouds with tops below about 3 km. These are expected to be predominantly shallow cumulus, which cover much of the undisturbed tropical oceans. Several observational campaigns, such as ATEX [*Augstein et al.*, 1973], BOMEX [*Holland and Rasmusson*, 1973], and RICO [*Rauber et al.*, 2007], have explored the structure of convection in the

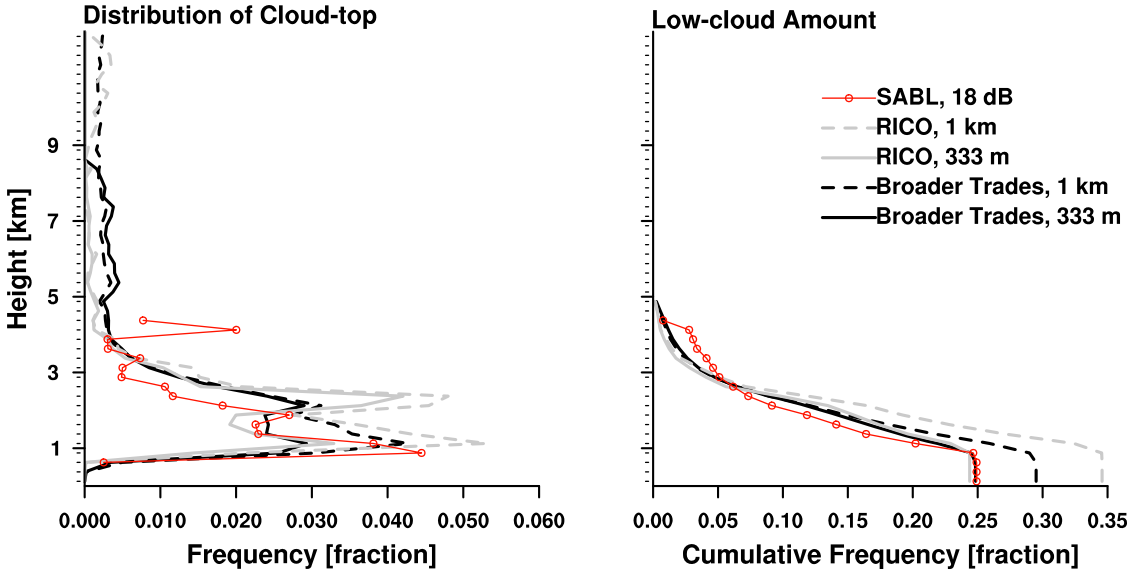

Figure 7. Comparison of SABL cloud detection defined with an 18 dB threshold (red line with circles) with the CALIPSO products for the RICO area (gray lines) and the broader trades (black lines). The lowest height bin in the SABL distribution is masked to eliminate noise introduced by the surface.

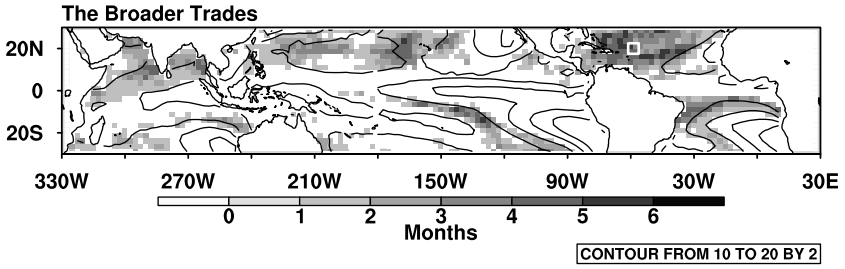

Figure 8. Location and frequency of conditions similar to those observed during RICO from ERA-Interim monthly means (gray scale, 6 months total). Contour lines show the mean lower-tropospheric stability over the same 6 months. The white square denotes the RICO site, i.e., the four 2.5° grid boxes immediately upstream of the Antigua and Barbuda.

trades; along with the simulations they have inspired (e.g., *Stevens et al.* [2001], *Siebesma et al.* [2003], and *Stevens and Seifert* [2008], respectively) these field studies largely inform our process understanding of shallow cumulus convection. The relatively detailed understanding of measurements from these programs may provide guidance in interpreting results from CALIPSO. If so, then we can hypothesize that the CALIPSO data can, in turn, be used to generalize results from field studies that are inherently limited in space and time.

[28] Figure 7 shows the distribution of cloud-top height from the SABL data collected during RICO (connected red circles). The cumulative distribution estimates cloud amount, and is shown in Figure 7 (right). The SABL measurements suggest low-cloud amount of around 25%. As mentioned above, this value depends on the choice of threshold in defining cloudy lidar returns. We find about a 2% dB^{-1} sensitivity near cloud base.

[29] Along with the SABL cloud-top height distribution, Figure 7 shows CALIPSO cloud-top height distributions with two sampling strategies. First, to concentrate on the same geographic area as the field study, we use the four nearest 2.5° × 2.5° grid boxes upstream of Antigua and Barbuda (see Figure 8); the distribution within the area is shown with gray curves in Figure 7. The CALIPSO distributions include all returns when one cloud layer is identified, so, as above, this shows the frequency of detecting a single cloud layer relative to detecting zero or multiple cloud layers. The 333 m and 1 km products are similar in shape, but the 1 km product shows more frequent cloud detection, as can be seen in the cumulative distribution (Figure 7, right).

[30] The CALIPSO and SABL distributions are similar, with indications of bimodal structure in the cloud layer. Maxima appear around 0.75–1 km and 2.0–2.5 km, with the SABL maxima lower than CALIPSO's. The lower maximum is near cloud base, and so may indicate detections of nascent clouds; large-eddy simulation suggests these are the smallest clouds but contribute strongly to the cloud fraction in the lower part of the cloud layer [*Neggers et al.*, 2003]. The higher peak is evocative of detrained liquid near the top of the cloud layer; such a feature has been observed in field campaigns [*Albrecht*, 1991; *Albrecht et al.*, 1995] and reproduced in simulations [*Bretherton et al.*, 1998]. Cloud top near 4 km was commonly observed during RICO, seen in the SABL distribution; the CALIPSO products do not show much evidence for cloud top at this height.

[31] The second sampling strategy shown in Figure 7 (black curves) enlarges the sample by using all 2.5° grid boxes with conditions similar to those observed during RICO. These can be considered the "broader trades," and are selected based on the monthly mean lower-tropospheric stability and vertical velocity from the ERA-Interim reanalysis. The criteria used are twofold, following *Medeiros and Stevens* [2010]: first, a dynamic constraint requiring subsiding motion through the lower troposphere (i.e., $\omega \geq 10$ hPa d^{-1} at 500 and 700 hPa), and second, a thermodynamic constraint that requires the lower-tropospheric stability to match that of radiosondes launched during RICO ($12.26\text{K} \leq \text{LTS} \leq 14.14\text{K}$, which is the mean value $\pm 0.5\sigma$). Figure 8 shows the frequency and location of these conditions along with the lower-tropospheric stability. Table 1 shows that there are about 30 times more returns across the broader trades than when using just the RICO site.

[32] The broader trades show similar characteristics to the RICO area; the differences being that the RICO site shows more frequent single-cloud layers below 3 km and somewhat smaller frequency above 5 km. Both sampling strategies are similar to the tropical oceans (Figure 4), though the bimodality within the low-cloud layer is more pronounced in the smaller samples.

[33] Estimates of the low-cloud amount from the broader trades is also consistent with the SABL distribution. The 1 km product consistently produces larger estimates of low-cloud amount, and the departure from the 333 m product appears most pronounced near cloud base. This might signal a bias in the 1 km product, perhaps arising from misidentifying layers of deliquesced aerosol as thin cloud. Figure 4 also shows this discrepancy and suggests that the difference is larger in the daytime.

[34] Sampling based on the large-scale conditions seems to provide an analog to geographic sampling [cf. *Medeiros and Stevens* 2010], with the advantage of larger sample size. The extent of the analog depends on the selection criteria; the criteria used here, for example, seem to allow some elevated cloud layers into the sample, which may be a consequence of using the monthly mean large-scale conditions to sample the instantaneous CALIPSO products. With such caveats in mind, the similarities between the aircraft-based measurements and the space-based distributions are

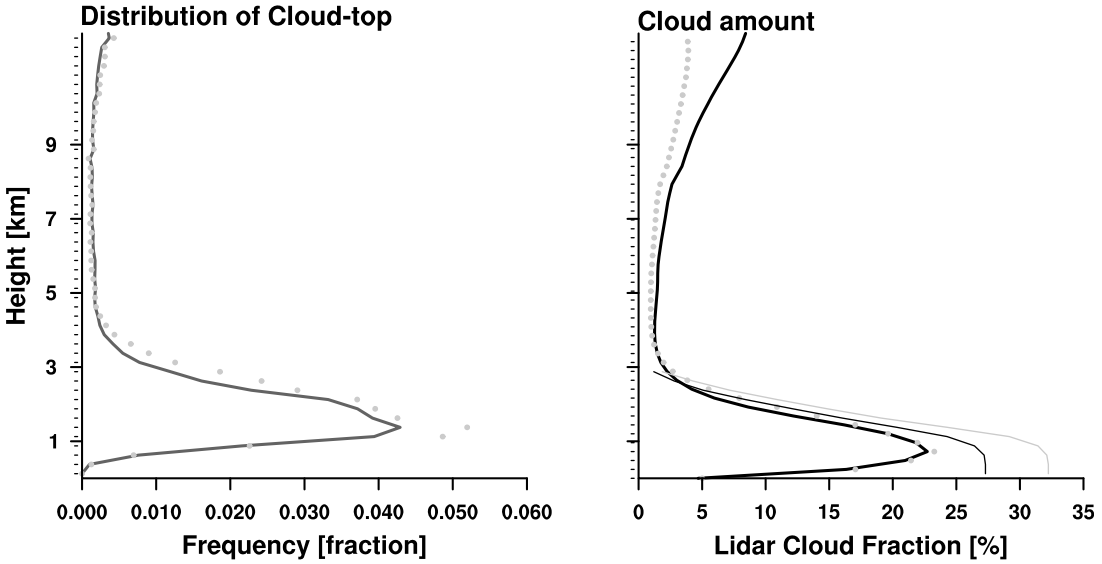

Figure 9. (left) Cloud top distribution from RL-GEOPROF for tropical ocean (solid line) and the broader trades (circles). (right) Lidar cloud fraction from RL-GEOPROF (as in Figure 9, left), and cumulative cloud top distribution (thin curves). The cloud top distributions show the frequency of occurrence of one cloud layer versus any number of layers (as in Figure 4). The average lidar cloud fraction is calculated using only zero and one cloud layers, discarding multilayer detections (standardizing by the total number reduces the maximum cloud fraction to 15–20%).

substantial, which encourages generalizations based on the RICO measurements.

5. Comparison With a Radar/Lidar Product

[35] Figure 9 shows the vertical distribution of cloud top from the RL-GEOPROF combined radar/lidar product when a single cloud layer is identified. Again we see the dominance of low-level clouds over the tropical oceans (solid curve) and the similarity to the broader trades (markers), in agreement with the CALIPSO distributions (e.g., Figures 4 and 7). This agreement between RL-GEOPROF and CALIPSO is no surprise: low-level tropical clouds tend to be under relatively clear skies where the lidar is most reliable, and the RL-GEOPROF algorithm defers to the lidar whenever possible to define layer boundaries. The cumulative cloud-top distribution estimates the low-cloud amount, shown by thin curves in Figure 9 (right). The RL-GEOPROF product is less reliable in the lowest 1 km because of the size of the radar pulse [*Marchand et al.*, 2008; *Mace et al.*, 2009], and including the lowest 1 km slightly increases the low-cloud amount (by about 3%).

[36] The RL-GEOPROF includes the lidar cloud fraction, defined as the fraction of lidar volumes detecting cloud within a radar volume, shown in the right panel of Figure 9. The lidar cloud fraction may underestimate cloud fraction in thick cloud layers because of attenuation of the lidar signal. *Mace et al.* [2009] compensate for attenuation by using this lidar cloud fraction along with the CloudSat radar cloud mask to construct a combined cloud mask (defined by lidar cloud fraction $\geq$ 50% or radar cloud mask values $\geq$ 20). Figure 9 shows simply the average lidar cloud fraction without using any radar cloud information. Nonzero values of lidar cloud fraction tend to be high, usually meeting the *Mace et al.* [2009] criterion; values in Figure 9 are reduced to realistic cloud fractions by including the zero-layer detections.

[37] The average lidar cloud fraction profiles, for both the whole tropical ocean and the broader trades, reflect the expected cloud structure. Across the broader trades, shallow cumulus should prevail, and cloud fraction is expected to maximize near cloud base and decrease toward cloud top [e.g., *Siebesma et al.*, 2003]; this is the picture that emerges from Figure 9. Using only lidar data, however, may introduce attenuation effects in cloudy air, as shown in examples by *Kahn et al.* [2008] and *Mace et al.* [2009]. The cumulative cloud-top distributions (thin curves in Figure 9, right) show greater cloud coverage, though the application of a maximum overlap assumption will overestimate cloudiness. These approaches appear to provide reasonable bounds on the cloud amount as measured by the RL-GEOPROF technique. Including information from the radar cloud mask, as in work by *Mace et al.* [2009], reduces attenuation effects, but is also likely to increase the frequency of detecting hydrometeor layers and result in larger cloud amount.

[38] These estimates of low-cloud amount (Figure 9) are consistent with the CALIPSO-only and SABL measurements. They are, however, larger than some estimates of cloud fraction in the trades. *Zhao and Di Girolamo* [2007], for example, report 8.6% from ASTER scenes near the RICO site during late 2004. This large discrepancy might arise from any number of differences, including intrinsic differences in instrumentation and detection methods between ASTER and CALIPSO, analysis methods, or differences in the clouds sampled. In their analysis, *Zhao and Di Girolamo* [2007] employ stringent criteria to ensure only cumulus clouds are analyzed while we endeavor to retain as much data as possible, making it likely that we include clouds that would have been excluded from their study. Late

2004 has also been noted for particularly suppressed conditions in the western Atlantic, which could account for some of the difference. On the other hand, the ISCCP D2 product contains relatively large cloud amounts. Sampling the broader trades for December 2006 to February 2007, the ISCCP low-cloud amount is 30.1% (a similar value is obtained for all tropical ocean areas). Thus, our estimates of low-cloud amount across the broader trades appears to be within the range of other estimates, though that range is quite wide. It is worth keeping in mind that cloud amount is not a well defined quantity, and the range of estimates is partly a measure of how sensitive clouds are to different detection criteria.

6. Summary and Conclusions

[39] This study explores the emerging climatology of tropical clouds from the lidar aboard CALIPSO using the 333 m and 1 km cloud products. The CALIPSO products are shown to detect regional patterns of cloud cover that are similar to other cloud data sets (e.g., ISCCP). The advantage of the lidar is demonstrated by the distribution of cloud-top height, which shows that the tropical ocean is dominated by clouds with tops below 3 km. In contrast, clouds over tropical land tend to have higher tops, and are more strongly affected by diurnal variation in convection. Similar distributions are found using a combined CloudSat-CALIPSO product (RL-GEOPROF). Both CALIPSO products, and to a lesser extent the RL-GEOPROF, are found to be consistent with lidar measurements from the RICO field study. We find that the structure of the clouds in the RICO domain is similar across the broader trades, and we suggest this is evidence that conclusions drawn from detailed observations during RICO are relevant to trade-wind clouds in general.

[40] The 1 km and 333 m CALIPSO products produce similar cloud distributions, but we find that both products also seem to have some biases. Most prominent are the issues involving the limitation of the 333 m product in the vertical. This product is constructed such that there is no distinction between clear sky and cloud above 8.2 km. The 1 km product can detect cloud above 8.2 km, resulting in higher frequency of cloud detection and more multilayer detections while the 333 m product has an overabundance of zero-layer detections. These differences are most apparent in regions of optically thick high clouds, often associated with deep convection, but are even noticeable in the subtropics. We also find that the 333 m product has a proclivity to identify cloud layers close to each other in the vertical. The 1 km product reports more cloud than the 333 m product, especially near cloud base, which may indicate the algorithm sometimes misclassifies deliquesced aerosol layers as cloud.

[41] Estimates of low-cloud amount from both products are larger than some satellite-based estimates in the trades [*Zhao and Di Girolamo*, 2007], but similar to, or smaller than, others (e.g., ISCCP). The RL-GEOPROF cloud-top distribution is consistent with the CALIPSO-only estimates (about 25–30%), but the lidar cloud fraction suggests slightly smaller values (around 23%). The RICO lidar measurements suggest low-cloud amount around 25%; the 333 m product agrees with this value while the 1 km product finds more cloud. Thus the 333 m product appears to well represent the structure of the cloud layer, while the 1 km product probably overestimates cloud amount.

[42] The comparison between the CALIPSO products and field measurements are expanded to the broader trades by sampling large-scale conditions similar to those observed during RICO. We show that this sampling preserves the similarity between the satellite and aircraft-based cloud distributions. This implies that the structure of the trade-wind clouds observed during RICO, and near the RICO site, is similar to the structure across the broader trades. Findings from detailed field observations are thus likely to be relevant at larger scales. Such regime-based approaches improve statistics by enlarging the sample, and can also be used to better constrain the physical parameterizations of numerical models.

[43] **Acknowledgments.** ECMWF ERA-Interim data used in this study have been obtained from the ECMWF data server. This work has been supported by the National Science Foundation Science and Technology Center for Multi-Scale Modeling of Atmospheric Processes, managed by Colorado State University under cooperative agreement ATM-0425247 and by the Office of Science (BER), U.S. Department of Energy, cooperative agreement DE-FC02-97ER62402. The National Center for Atmospheric Research is sponsored by the National Science Foundation.

References

Albrecht, B. A. (1991), Fractional cloudiness and cloud-top entrainment instability, *J. Atmos. Sci.*, *48*(12), 1519–1525.

Albrecht, B. A., C. S. Bretherton, D. Johnson, W. S. Schubert, and A. S. Frisch (1995), The Atlantic stratocumulus transition experiment – ASTEX, *Bull. Am. Meteorol. Soc.*, *76*, 889–904.

Augstein, E., H. Riehl, F. Ostapoff, and V. Wagner (1973), Mass and energy transports in an undisturbed Atlantic trade-wind flow, *Mon. Weather Rev.*, *101*, 101–111.

Bony, S., J.-L. Dufresne, H. L. Treut, J.-J. Morcrette, and C. Senior (2004), On dynamic and thermodynamic components of cloud changes, *Clim. Dyn.*, *22*, 71–86.

Bretherton, C. S., S. K. Krueger, M. C. Wyant, P. Bechtold, E. van Meijgaard, B. Stevens, and J. Teixeira (1998), A GCSS boundary layer cloud model intercomparison study of the first ASTEX Lagrangian experiment, *Boundary Layer Meteorol.*, *93*, 341–380.

Cess, R., et al. (1989), Interpretation of cloud-climate feedback as produced by 14 atmospheric general circulation models, *Science*, *245*, 513–516.

Hartmann, D. L., M. E. Ockert-Bell, and M. L. Michelsen (1992), The effect of cloud type on Earth's energy balance: Global analysis, *J. Clim.*, *5*(11), 1281–1304.

Haynes, J. M., and G. L. Stephens (2007), Tropical oceanic cloudiness and the incidence of precipitation: Early results from CloudSat, *Geophys. Res. Lett.*, *34*, L09811, doi:10.1029/2007GL029335.

Holland, J. Z., and E. M. Rasmusson (1973), Measurements of the atmospheric mass, energy, and momentum budgets over a 500-kilometer square of tropical ocean, *Mon. Weather Rev.*, *101*, 44–55.

Kahn, B. H., et al. (2008), Cloud type comparisons of AIRS, CloudSat, and CALIPSO cloud height and amount, *Atmos. Chem. Phys.*, *8*(5), 1231–1248.

Leon, D. C., Z. Wang, and D. Liu (2008), Climatology of drizzle in marine boundary layer clouds based on 1 year of data from CloudSat and Cloud-Aerosol Lidar and Infrared Pathfinder Satellite Observations (CALIPSO), *J. Geophys. Res.*, *113*, D00A14, doi:10.1029/2008JD009835 [printed 114(D8), 2009].

Mace, G. G., Q. Zhang, M. Vaughan, R. Marchand, G. Stephens, C. Trepte, and D. Winker (2009), A description of hydrometeor layer occurrence statistics derived from the first year of merged Cloudsat and CALIPSO data, *J. Geophys. Res.*, *114*, D00A14, doi:10.1029/2008JD009835.

Marchand, R., G. G. Mace, T. Ackerman, and G. Stephens (2008), Hydrometeor detection using CloudSat—An Earth-orbiting 94-GHz cloud radar, *J. Atmos. Oceanic Technol.*, *25*(4), 519–533.

Medeiros, B., and B. Stevens (2010), Revealing differences in GCM representations of low clouds, *Clim. Dyn.*, doi:10.1007/s00382-009-0694-5, in press.

Medeiros, B., B. Stevens, I. M. Held, M. Zhao, D. L. Williamson, J. G. Olson, and C. S. Bretherton (2008), Aquaplanets, climate sensitivity, and low clouds, *J. Clim.*, *21*(19), 4974–4991.

Neggers, R. A. J., H. J. J. Jonker, and A. P. Siebesma (2003), Size statistics of cumulus cloud populations in large-eddy simulations, *J. Atmos. Sci.*, *60*(8), 1060–1074.

Neggers, R. A. J., J. D. Neelin, and B. Stevens (2007), Impact mechanisms of shallow cumulus convection on tropical climate dynamics, *J. Clim.*, *20* (11), 2623–2642.

Nuijens, L., B. Stevens, and A. P. Siebesma (2009), The environment of precipitating shallow cumulus convection, *J. Atmos. Sci.*, *66*(7), 1962–1979.

Rauber, R. M., et al. (2007), Rain in Shallow Cumulus Over the Ocean: The RICO campaign, *Bull. Am. Meteorol. Soc.*, *88*(12), 1912–1928.

Rossow, W. B., and R. A. Schiffer (1999), Advances in understanding clouds from ISCCP, *Bull. Am. Meteorol. Soc.*, *80*(11), 2261–2287.

Siebesma, A. P., et al. (2003), A large eddy simulation intercomparison study of shallow cumulus convection, *J. Atmos. Sci.*, *60*(10), 1201–1219.

Stephens, G. L., et al. (2002), The CloudSat Mission and the A-Train, *Bull. Am. Meteorol. Soc.*, *83*(12), 1771–1790.

Stevens, B., and A. Seifert (2008), Understanding macrophysical outcomes of microphysical choices in simulations of shallow cumulus convection, *J. Meteorol. Soc. Jpn.*, *86A*, 143–162.

Stevens, B., et al. (2001), Simulations of trade-wind cumuli under a strong inversion, *J. Atmos. Sci.*, *58*(14), 1870–1891.

Vaughan, M., S. Young, D. Winker, K. Powell, A. Omar, Z. Liu, Y. Hu, and C. Hostetler (2004), Fully automated analysis of space-based lidar data: An overview of the CALIPSO retrieval algorithms and data products, *Proc. SPIE Int. Soc. Opt. Eng.*, *5575*, 16–30.

Vaughan, M. A., K. A. Powell, D. M. Winker, C. A. Hostetler, R. E. Kuehn, W. H. Hunt, B. J. Getzewich, S. A. Young, Z. Liu, and M. J. McGill (2009), Fully automated detection of cloud and aerosol layers in the CALIPSO lidar measurements, *J. Atmos. Oceanic Technol.*, *26* (10), 2034–2050.

Winker, D. M., J. Pelon, and M. P. McCormick (2003), The CALIPSO mission: Spaceborne lidar for observation of aerosols and clouds, *Proc. SPIE Int. Soc. Opt. Eng.*, 1–11.

Winker, D., B. Getzewitch, and M. Vaughan (2008), Evaluation and applications of cloud climatologies from CALIOP, paper presented at 24th International Laser Radar Conference, Natl. Cent. for Atmos. Res., Boulder, Colo.

Winker, D. M., M. A. Vaughan, A. Omar, Y. Hu, K. A. Powell, Z. Liu, W. H. Hunt, and S. A. Young (2009), Overview of the CALIPSO mission and CALIOP data processing algorithms, *J. Atmos. Oceanic Technol.*, *26*(11), 2310–2323.

Wu, D., et al. (2009), Vertical distribution and relationships of cloud occurrence frequency as observed by MISR, AIRS, MODIS, OMI, CALIPSO, and CloudSat, *Geophys. Res. Lett.*, L09821, doi:10.1029/2009GL037464.

Zhao, G., and L. Di Girolamo (2007), Statistics on the macrophysical properties of trade wind cumuli over the tropical western Atlantic, *J. Geophys. Res.*, *112*, D10204, doi:10.1029/2006JD007371.

C. Antoniazzi and L. Nuijens, Department of Atmospheric and Oceanic Sciences, University of California, Los Angeles, CA 90095, USA. (chiaraantoniazzi@hotmail.com; lnuyens@atmos.ucla.edu)

B. Medeiros, Climate and Global Dynamics, National Center for Atmospheric Research, Boulder, CO 80307, USA. (brianpm@ucar.edu)

B. Stevens, Max Planck Institute for Meteorology, Bundesstr. 53, D-20146 Hamburg, Germany. (bjorn.stevens@zmaw.de)